ARTICLE   OPEN

Observationally constrained aerosol–cloud semi-direct effects

Robert J. Allen [1], Anahita Amiri-Farahani[1], Jean-Francois Lamarque [2], Chris Smith [3], Drew Shindell [4], Taufiq Hassan[1] and Chul E. Chung [5]

Absorbing aerosols, like black carbon (BC), give rise to rapid adjustments, and the associated perturbation to the atmospheric temperature structure alters the cloud distribution. The level of scientific understanding of these rapid cloud adjustments—otherwise known as semi-direct effects (SDEs)—is considered low, with models indicating a likely negative (-0.44 to $+0.1$ Wm^{-2}) forcing. Recent studies suggest this negative SDE is primarily driven by decreases in high-level clouds and enhanced longwave cooling. Here, we investigate the SDE using multiple models driven by observationally constrained fine-mode aerosol forcing without dust and sea salt. Unlike aerosol simulations, which yield a relatively vertically uniform aerosol atmospheric heating profile with significant upper-tropospheric heating, observation-based heating peaks in the lower-troposphere and then decays to zero in the mid-troposphere. We find a significant global annual mean decrease in low- and mid-level clouds, and weaker decreases in high-level clouds, which leads to a positive SDE dominated by shortwave radiation. Thus, in contrast to most studies, we find a robust positive SDE, implying cloud adjustments act to warm the climate system. Sensitivity tests with identical average, but vertically uniform observationally constrained aerosol atmospheric heating result in a negative SDE, due to enhanced longwave cooling as a result of large reductions in high-level clouds. Our results therefore suggest that model simulations lead to a negatively biased SDE, due to an aerosol atmospheric heating profile that is too vertically uniform.

INTRODUCTION

Unlike other climate change drivers, the temperature and cloud response—and in some cases, the precipitation response[1]—to absorbing aerosol is dominated by rapid adjustments.[2] Recent modeling studies suggest that these adjustments, which include the aerosol–cloud semi-direct effect (SDE), lead to a negative radiative perturbation, thereby offsetting some of the positive direct forcing of absorbing aerosol, resulting in a relatively weak surface temperature response.[2–4] Climate models from the Precipitation Driver Response Model Intercomparison Project (PDRMIP) show that a tenfold increase in BC leads to a robust increase in globally averaged low-level cloud, but a reduction in mid-level and in particular, high-level cloud.[2] These responses are consistent with the simulated vertical co-location of absorbing aerosol and cloud, including relative humidity reductions and cloud burn-off when BC and cloud are co-located,[5,6] but also enhanced low-level cloud due to increases in stability when BC is located above the cloud.[7–11] Qualitatively similar cloud responses are obtained in several other recent studies.[12–14] Consistent with these cloud changes, and in particular the large high-cloud reduction and enhanced longwave cooling, the annual global mean rapid adjustment in these simulations ranges from -0.39 to -1.44 W m^{-2} for a tenfold increase in BC;[2,12] -2.8 W m^{-2} for 25 × BC;[14] and -0.25 W m^{-2} for present-day BC emissions.[13] Thus, model simulations indicate that rapid adjustments—primarily due to cloud responses—offset up to 60% of the direct radiative forcing associated with BC.[2]

The climate impact of absorbing aerosols, however, is associated with significant uncertainty.[15,16] This is related to several factors, including underestimation of BC emission inventories and absorption aerosol optical depth, which implies too little aerosol solar absorption in the atmosphere and therefore, underestimation of BC direct radiative forcing.[15,17–21] The vertical profile of absorbing aerosol is also important, as it impacts the direct radiative forcing, as well as the rapid adjustments and precipitation response.[9,15,18,22–25] In the context of the aerosol–cloud SDE, different cloud responses are obtained depending on the vertical co-location of absorbing aerosol and cloud.[9,15,26]

Large inter-model diversity exists in simulated BC vertical profiles, with models likely overestimating the amount of BC aloft.[15,18,27,28] This could be related to a variety of factors, including vertical resolution,[29] convective processes,[28,30] scavenging,[31] or aging.[32] Thus, given these uncertainties in aerosol simulations—particularly related to the vertical profile of absorbing aerosol—the corresponding aerosol–cloud SDE may not be properly constrained by the aforementioned studies.

Aerosol observations, including the Cloud–Aerosol Lidar with Orthogonal Polarization (CALIOP)[33] allow the the aerosol vertical profile to be constrained. Here, we estimate the aerosol–cloud SDE using three different climate models (Methods), including the Community Atmosphere Model version 4 (CAM4)[34] and CAM5,[35] as well as the Geophysical Fluid Dynamics Laboratory (GFDL) Atmospheric Model version 2.1 (AM2.1),[36] forced with monthly observationally constrained fine-mode aerosols without dust and sea salt[37] (Methods; STANDARD simulations). Unlike the anthropogenic fraction, the fine-mode fraction of aerosol amount—which is largely anthropogenic—can be constrained by observations. We also conduct analogous observationally constrained

[1]Department of Earth Sciences, University of California Riverside, Riverside, CA 92521, USA; [2]NCAR/UCAR, Boulder, CO, USA; [3]Priestley International Centre for Climate, University of Leeds, Leeds LS2 9JT, UK; [4]Earth and Ocean Sciences Division, Duke University, Durham, NC, USA and [5]Division of Atmospheric Science, Desert Research Institute, Reno, NV 89512, USA
Correspondence: Robert J. Allen (rjallen@ucr.edu)

aerosol simulations, but with [a.] vertically uniform aerosol atmospheric heating (VERTUNIF simulations) and [b.] half the forcing (i.e., monthly surface reduction in solar radiation and atmospheric solar heating reduced by 50%; HALF simulations). These simulations are compared with PDRMIP 10xBC aerosol simulations (Methods). We do not attempt to quantify inter-annnual variability, instead focusing on the climatological mean signal. However, there is a considerable year-to-year variability in biomass burning, which implies similarly large internannual variability in the aerosol–cloud semi-direct effect.

RESULTS

Observationally constrained fine-mode aerosols

Figure 1 shows the annual mean atmospheric solar absoprtion (F_{ATM}) and reduction in surface solar radiation (F_{SFC}) for observationally constrained fine-mode aerosols, without dust

and sea salt. The maximum atmospheric heating occurs over central Africa (due to biomass burning), India (due to biofuel burning and fossil fuel combustion), and China (due to fossil fuel combustion). The sunlight absorption by aerosols comes largely from BC, but brown carbon (or organic aerosols) also contributes to the absorption. Figure 1 also shows the vertical profile of the atmospheric solar heating rate response in CAM4 STANDARD (other models are similar). Most of the heating occurs near the surface, peaking at ~925 hPa, and then rapidly decaying to zero near ~500 hPa. Although aerosol simulations generally reproduce a similar spatial distribution of F_{SFC} and F_{ATM}, their vertical aerosol heating profile is more uniform, with relatively large heating that extends through the upper troposphere.[2] Based on PDRMIP 10xBC simulations, the atmospheric solar heating response remains relatively large up to 100 hPa, with most models exhibiting a secondary peak near 200 hPa (Fig. 1c). The percent of average shortwave heating above 500 hPa, relative to the column average,
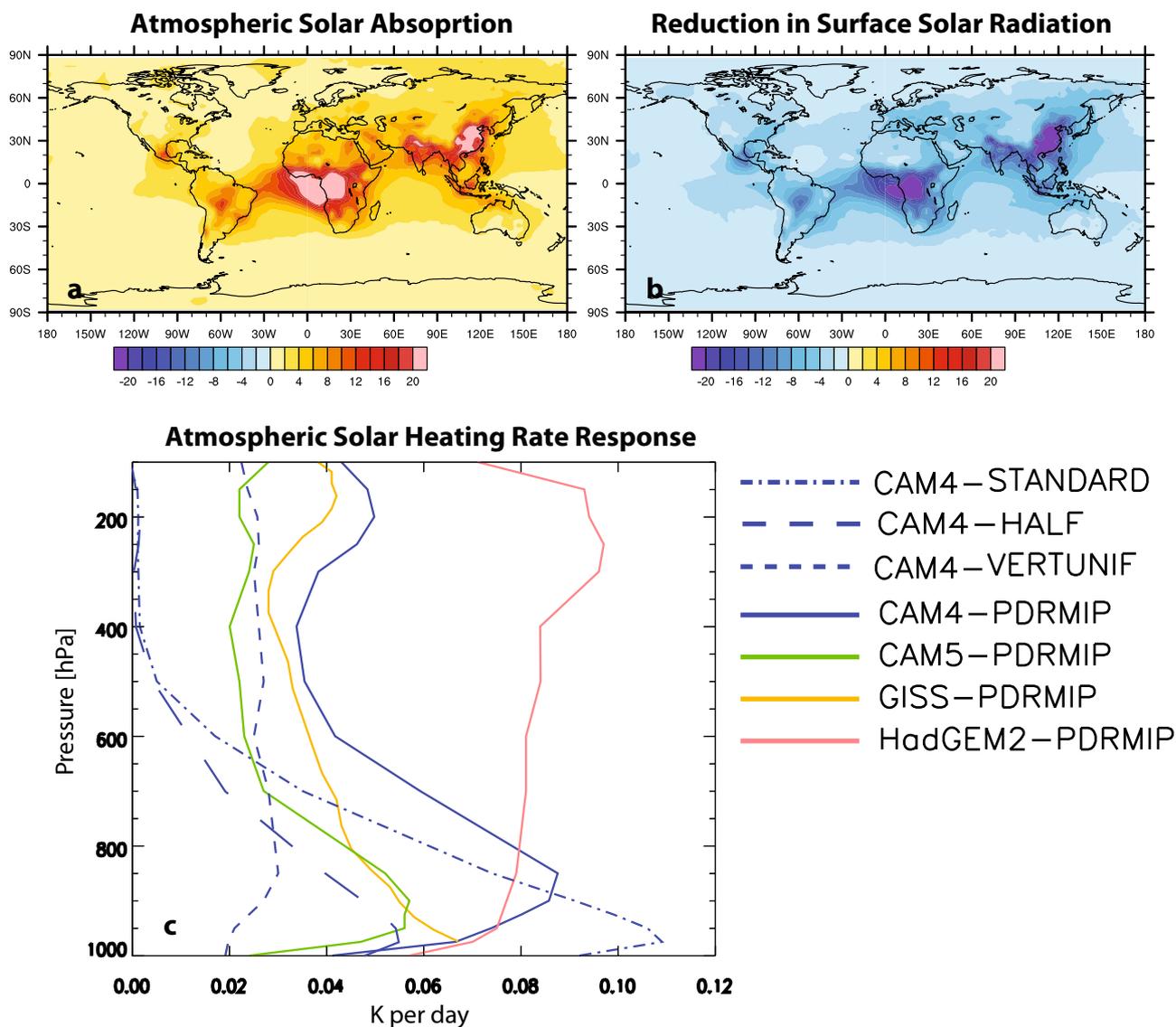
Fig. 1 Annual mean observationally constrained fine-mode aerosol forcing without dust and sea salt. Spatial maps of **a** atmospheric solar absorption and **b** reduction in surface solar radiation. **c** Global mean vertical profile of the corresponding atmospheric solar heating rate response in CAM4 with observationally constrained fine-mode aerosol forcing without dust and sea salt (STANDARD). Also included is the corresponding heating rate response in CAM4 with the same observationally constrained fine-mode aerosol forcing, but with vertically uniform aerosol atmospheric heating (VERTUNIF) and with the reduction in surface solar radiation and atmospheric solar absorption reduced by 50% (HALF). PDRMIP 10xBC simulations are also included (only four PDRMIP models archived the shortwave heating rate). Units are W m^{-2} for **a**, **b** and K day^{-1} for **c**

ranges from 70% in CAM5-PDRMIP to 110% in HadGEM2, with a multi-model PDRMIP mean of 86%. This is considerably larger than that based on the observationally constrained heating profile, at 2% (by design, VERTUNIF yields 100%). Moreover, the lower-tropospheric heating maximum is elevated relative to observationally constrained fine-mode aerosols (~850 vs. 925 hPa). These large differences in simulated versus observed vertical aerosol heating profile imply corresponding differences in the aerosol–cloud SDE (i.e., cloud adjustment).

Cloud responses

Figure 2a shows global annual mean vertical profiles of the cloud response to observationally constrained fine-mode aerosol forcing without dust and sea salt (STANDARD). Weak increases occur near the surface (especially in CAM4), which then give way to much larger decreases that span the entire troposphere, extending from ~950 to 250 hPa. Consistently, all models show global annual mean cloud reductions for low-, mid-, and high-level clouds (Methods), with the largest decreases in low- and mid-level clouds (Table 1). The annual mean low cloud response varies between −0.43% in GFDL to −0.14% in CAM4. The annual mean mid-level (high) cloud response varies from −0.26% in CAM4 to −0.21% in GFDL (−0.04% in GFDL to −0.12 % in CAM5). Figure 2b shows that

these cloud responses are consistent with the corresponding change in relative humidity (RH). All three models show weak increases in RH near the surface, which then transitions into larger decreases in RH throughout most of the troposphere.

Across the three models, similar spatial cloud responses exist in several regions. Figure 3 shows low clouds generally increases over areas with large atmospheric heating, including Africa and parts of southeast Asia (Supplementary Fig. 1 shows model agreement). Low-cloud reductions occur over Indonesia, the Indian Ocean, and parts of the Northern Hemisphere mid- and high latitudes. Generally, similar signed cloud responses occur over both land and ocean, except for high-level cloud, which increases over land, but decreases over ocean in all models. The bulk of this high cloud increase occurs over central Africa, and is associated with an increase in vertical motion and convective mass flux, particularly in the upper troposphere (Supplementary Fig. 2). Although convective mass flux is generally reduced in response to the stabilizing effects of aerosol atmospheric heating —particularly in the lower troposphere—the large amount of atmospheric heating over Africa (Fig. 1) acts to destabilize the mid- and upper troposphere, resulting in rising air and an increase in high cloud. To a lesser extent, this is also the case over parts of southeast Asia.
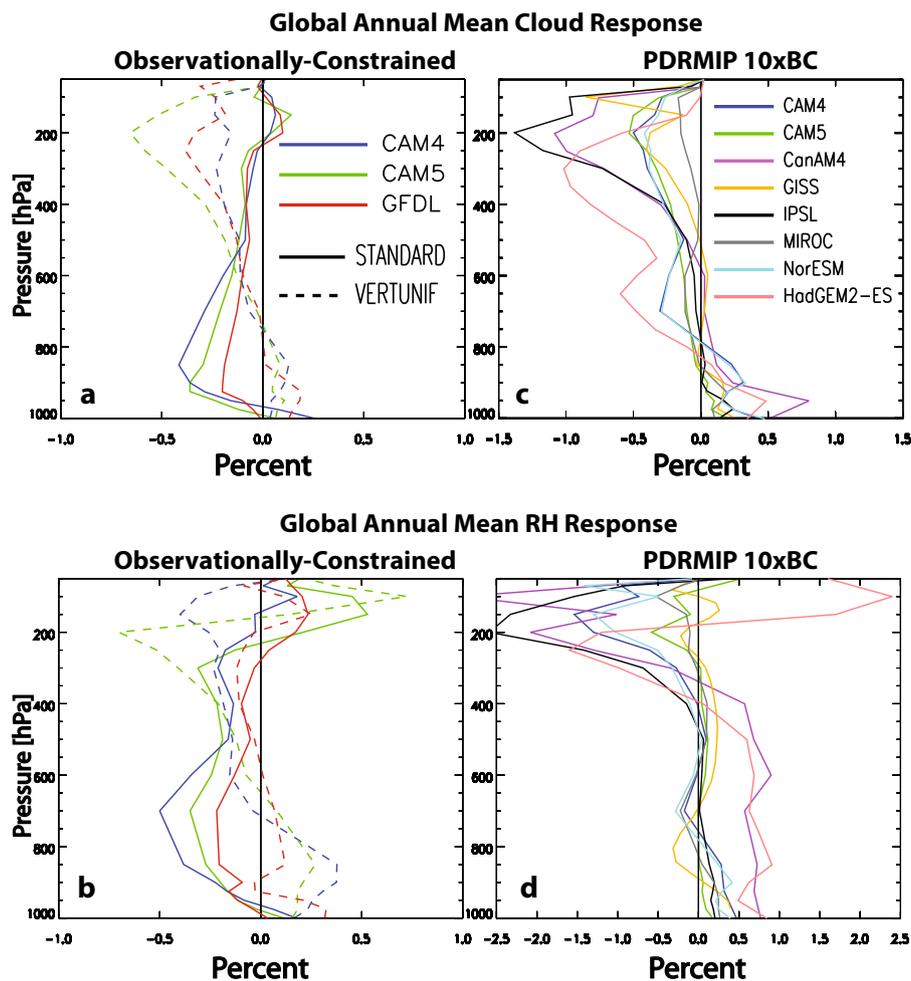
Fig. 2 Global annual mean vertical profiles of the cloud and relative humidity response. **a**, **c** Cloud and **b**, **d** relative humidity (RH) for (left panels) CAM4, CAM5, and GFDL AM2.1 forced with observationally constrained fine-mode aerosol forcing without dust and sea salt (STANDARD; solid); analogous simulations with vertically uniform aerosol atmospheric heating (VERTUNIF; dashed); and (right panels) PDRMIP 10xBC simulations. Units are %

Table 1. Global annual mean cloud changes and top-of-the-atmosphere radiative effects

Model	C_{BOT}	CLOW	CMED	CHI	ERF	RAP_{ADJ}	SDE	SDE_{SW}	SDE_{LW}
STANDARD									
CAM4	0.33	−0.14	−0.26	−0.07	0.21	0.32	0.29	0.46	−0.17
CAM5	0.07	−0.26	−0.22	−0.12	0.18	0.29	0.30	0.40	−0.10
GFDL	0.05*	−0.43	−0.21	−0.04*	0.32	0.43	0.52	0.67	−0.15
HALF									
CAM4	0.21	−0.02*	−0.13	−0.02*	0.08	0.14	0.14	0.22	−0.08
CAM5	0.01*	−0.18	−0.14	−0.11	0.10	0.15	0.17	0.22	−0.05
GFDL	0.04	−0.28	−0.13	0.02*	0.20	0.26	0.30	0.39	−0.08
VERTUNIF									
CAM4	0.10	0.25	−0.19	−0.54	−0.50	−0.39	−0.67	−0.17	−0.50
CAM5	0.09	0.21	−0.22	−0.80	−0.38	−0.27	−0.54	0.07*	−0.61
GFDL	0.11	0.18	−0.20	−0.71	−0.45	−0.34	−0.41	0.21	−0.62
PDRMIP									
CAM4-PDRMIP	0.40	0.11	−0.19	−0.30	0.76	−1.34	−1.05	−0.28	−0.77
CAM5-PDRMIP	0.11	0.07	−0.16	−0.31	0.30	−0.98	−1.14	−0.54	−0.60
HadGEM2-ES	0.07	0.03	−0.50	−0.42	2.91	−0.64	−1.26	0.31	−1.57
MIROC-SPRINTARS	0.10	0.05	−0.10	−0.09	0.67	−0.55	−0.41	−0.06	−0.35

Responses are shown for observationally constrained fine-mode aerosol forcing without dust and sea salt (STANDARD), analogous simulations with vertically uniform aerosol atmospheric heating (VERTUNIF) and PDRMIP models. Also included are simulations with the surface reduction in solar radiation and atmospheric solar heating reduced by 50% (HALF). Cloud changes are shown for the model's lowest level (C_{BOT}), as well as low-level (CLOW); mid-level (CMED); and high-level (CHI). Radiative effects include the effective radiative forcing (ERF); rapid adjustments (RAP_{ADJ}) and the aerosol–cloud semi-direct effect (SDE), which is also decomposed into shortwave (SDE_{SW}) and longwave (SDE_{LW}) components. RAP_{ADJ} is calculated as ERF–IRF, where IRF is the instantaneous radiative forcing (−0.11 W m^{-2} for STANDARD and −0.055 W m^{-2} for HALF). All changes are significant at the 90% confidence level, unless denoted with an asterisk. Cloud change units are %; ERF, RAP_{ADJ} and SDE units are W m^{-2}

An asterisk denotes changes that are not significant at the 90% confidence level

Mechanisms for cloud changes

All three models yield an increase in lower-tropospheric stability (S), primarily due to warming at 700 hPa (Supplementary Table 1; Supplementary Fig. 2). This increase in stability traps moisture near the surface, leading to a corresponding increase in near-surface RH and cloud, including significant increases in cloud and relative humidity at the model's bottom level. CAM4 yields the largest increase in cloud at the model's bottom level (Table 1), which is consistent with its S-based marine stratocumulus parameterization (Methods). However, above the near-surface, decreases in lower-tropospheric RH are consistent with an overall decrease in low cloud. For example, $RH_{925-700}$ decreases between −0.19 to −0.37% in GFDL and CAM4, respectively (Supplementary Table 1). Similarly, decreases in mid- and upper-tropospheric RH are consistent with decreases in mid and high cloud. $RH_{600-500}$ decreases between −0.09 to −0.25% in GFDL and CAM4; $RH_{300-250}$ decreases between −0.01 and −0.22% in GFDL and CAM5, respectively. A more detailed regression analysis (Supplementary Discussion; Supplementary Table 2) shows that RH is generally the best predictor, with S (vertical motion) also important for the low cloud (mid and high cloud) response (Supplementary Fig. 3). Thus, observationally constrained aerosol forcing yields overall cloud reductions, most of which is driven by decreases in RH and subsequent cloud burnoff.

The vertical profile of simulated climatological clouds differs in our models (Supplementary Fig. 4). For example, CAM5 shows the largest amount of cloud throughout the atmospheric column; GFDL shows the least amount of low-level cloud; and CAM4 shows the least amount of mid-level cloud. However, there does not seem to be a clear connection between the cloud response, and the amount of climatological cloud, implying parameterization differences (Methods) likely drive the bulk of any contrasting cloud responses in these models.

Semi-direct cloud responses and rapid adjustments

Figure 4a–c shows the aerosol–cloud SDE (Methods) for all three STANDARD simulations. All models yield a positive global annual mean SDE. The largest SDE occurs in GFDL at 0.52 W m^{-2}, followed by CAM5 and CAM4 at 0.30 and 0.29 W m^{-2}, respectively (Table 1). Similar (but smaller in magnitude) results exist for HALF (simulations with 50% less aerosol forcing). For example, GFDL yields an SDE of 0.30 W m^{-2}, followed by CAM5 and CAM4 at 0.17 and 0.14 W m^{-2}, respectively (Table 1). Thus, HALF simulations generally yield an SDE about 50% as large as in STANDARD. Several regions of SDE model agreement exist, including the Indian Ocean, most of south America, and parts of the NH mid-latitudes (Fig. 5a). Moreover, the SDE is dominated by shortwave effects, which drive the positive SDE; longwave effects act to mute the positive SDE. These changes are consistent with the corresponding changes in clouds. Low clouds tend to have a net cooling effect on the planet, due to high albedo; high clouds tend to have a net warming effect, due to their greenhouse effect. Mid-level clouds are a combination of both, but we find they tend to affect the SDE similarly to low-level clouds. Thus, the decrease in low- and mid-level cloud drives the positive SDE (in the shortwave), and the decrease in high-level clouds weakens this through enhanced longwave cooling. We also note that the rapid adjustments are positive in all models (Table 1), and dominated by the aerosol–cloud SDE. Although non-cloud adjustments (e.g., changes in temperature and moisture) also contribute to the rapid adjustments, this contribution is smaller (−0.09 to 0.03 W m^{-2} in STANDARD) than that due to cloud adjustments.

In contrast, several recent studies have shown the rapid adjustments (RAP_{ADJ}) to absorbing aerosol are negative.[2,4] PDRMIP 10xBC aerosol simulations yield a multi-model mean rapid adjustment of −0.94 W m^{-2}, ranging from −0.55 to −1.48 W m^{-2}, similar to previously published values.[2] Additional

STANDARD
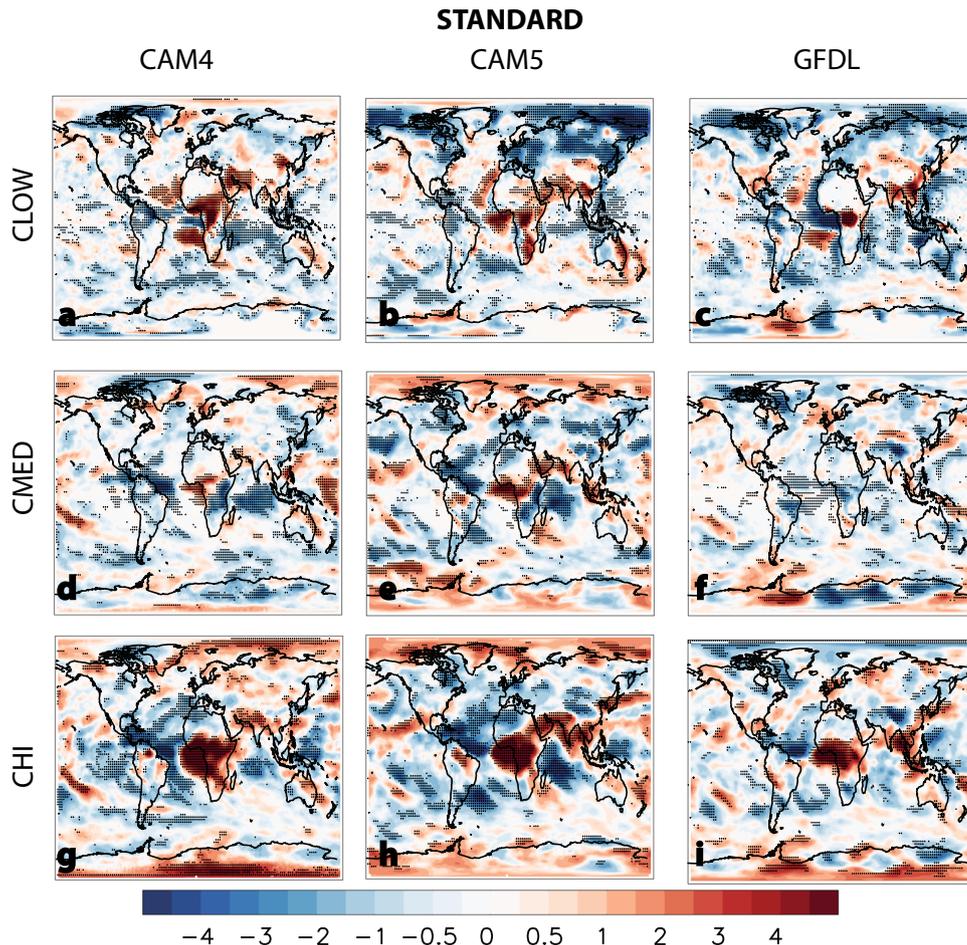
Fig. 3 Annual mean cloud response to observationally constrained fine-mode aerosol forcing without dust and sea salt. **a–c** Low-level (CLOW); **d–f** mid-level (CMED); and **g–i** high-level (CHI) cloud response for (left panels) CAM4; (center panels) CAM5; and (right panels) GFDL AM2.1 STANDARD simulations. Symbols denote significance at the 90% confidence level. Significance is based on a Student's *t* test for the difference of means, using the pooled variance. Units are %

analyses reveals that the rapid adjustment is dominated by the longwave component, with a multi-model mean of $-1.05 \, \text{W m}^{-2}$, ranging from -0.45 to $-2.24 \, \text{W m}^{-2}$ (Supplementary Table 3). The corresponding multi-model mean shortwave component is 0.12 (-0.22 to 0.76) W m^{-2}. The importance of longwave radiation to the rapid adjustment is consistent with the corresponding cloud changes (Fig. 2c). PDRMIP models yield increases in low cloud (0.07; 0.03 to 0.11%), decreases in mid-level cloud (-0.17; -0.50 to 0.02%), and most importantly, relatively large decreases in high cloud (-0.37; -0.79 to -0.09%), which is consistent with the negative RAP$_{\text{ADJ–LW}}$. Furthermore, PDRMIP cloud responses are consistent with the corresponding RH change (Fig. 2d). Although PDRMIP models show smaller decreases in high cloud over land (including increases over Africa and parts of India/southeast Asia), as compared with ocean, high cloud decreases over both ocean and land.

Unfortunately, most PDRMIP models did not archive the relevant diagnostics to quantify the importance of the aerosol–cloud SDE to the rapid adjustment. Calculation of the shortwave cloud forcing due to absorbing aerosol using standard techniques leads to a positive bias (in the shortwave), by increasing the radiative warming when the absorbing aerosol lies above clouds.[38] Thus, it is necessary to use either the clean sky cloud radiative forcing or the clear-sky instantaneous radiative forcing (IRF), and only four models archived these diagnostics (Methods). These four PDRMIP 10xBC simulations yield an aerosol–cloud SDE ranging from -0.41 to $-1.26 \, \text{W m}^{-2}$, with a multi-model mean of $-0.97 \, \text{W m}^{-2}$ (Table 1). Moreover, the SDE is dominated by longwave radiation, with SDE$_{\text{LW}}$ ranging from -0.35 to $-1.57 \, \text{W m}^{-2}$, with a multi-model mean of $-0.82 \, \text{W m}^{-2}$. Thus, the aerosol–cloud SDE is a relatively large negative number in PDRMIP 10xBC simulations, dominated by longwave radiation. This agrees with the aforementioned cloud changes, and in particular, the large decrease in high cloud (Supplementary Table 3). Although this conclusion is consistent with a recent PDRMIP 10xBC study using alternative methodologies,[4] some discrepancies related to the magnitude of the cloud (and non-cloud) adjustment exist (Methods).

In addition to a negative cloud adjustment in PDRMIP 10xBC simulations, a negative non-cloud adjustment has also been reported (Methods).[4] STANDARD yields weak non-cloud adjustments that are also generally negative, ranging from $-0.09 \, \text{W m}^{-2}$ in GFDL to $-0.01 \, \text{W m}^{-2}$ in CAM5 and 0.03 W m^{-2} in CAM4. The dominant contribution to the negative non-cloud adjustment in PDRMIP is the tropospheric temperature adjustment (which is partially canceled out by the water vapor adjustment). The stratospheric temperature adjustment, however, is also reasonably large (and negative).[4] PDRMIP 10xBC simulations have much larger atmospheric warming than our simulations (Supplementary Fig. 5), and in particular, more upper tropospheric and stratospheric warming. Most PDRMIP models actually show maximum atmospheric warming in the upper troposphere/lower stratosphere, near ~100 hPa (HadGEM2-ES being the exception). This is

Aerosol-Cloud Semi-Direct Effect
STANDARD
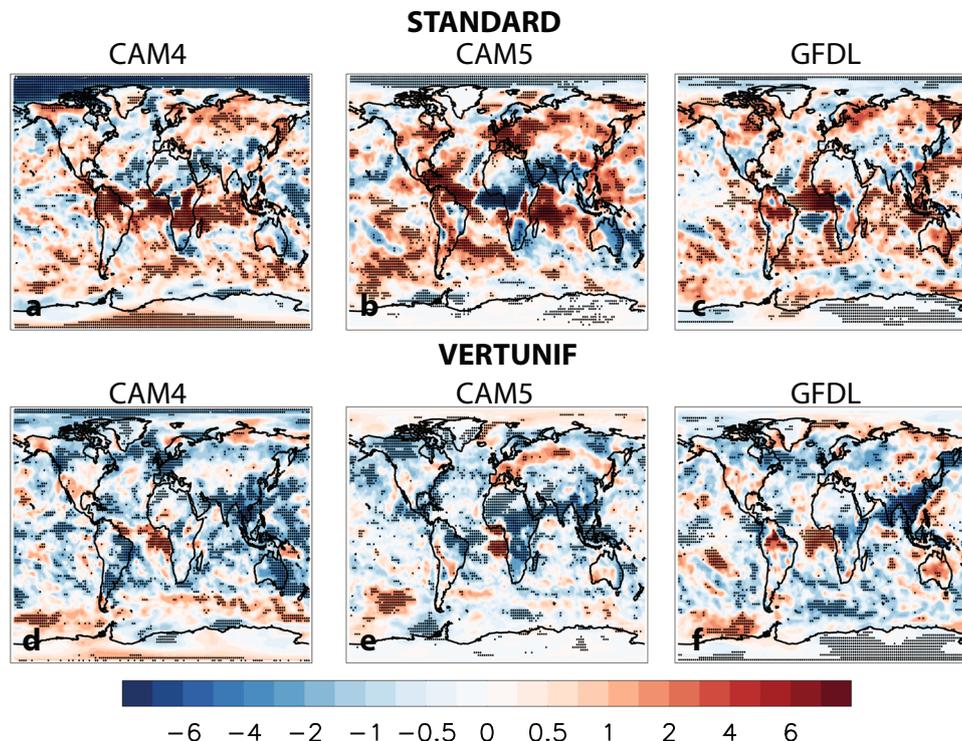
Fig. 4 Annual mean aerosol–cloud semi-direct effect. Semi-direct effect (SDE) based on (a–c) observationally constrained fine-mode aerosol forcing without dust and sea salt (STANDARD); d–f analogous simulations with vertically uniform aerosol atmospheric heating (VERTUNIF) for CAM4, CAM5, and GFDL AM2.1. Symbols denote significance at the 90% confidence level. Significance is based on a Student's t test for the difference of means, using the pooled variance. Units are W m^{-2}

Model Agreement
Semi-Direct Effect
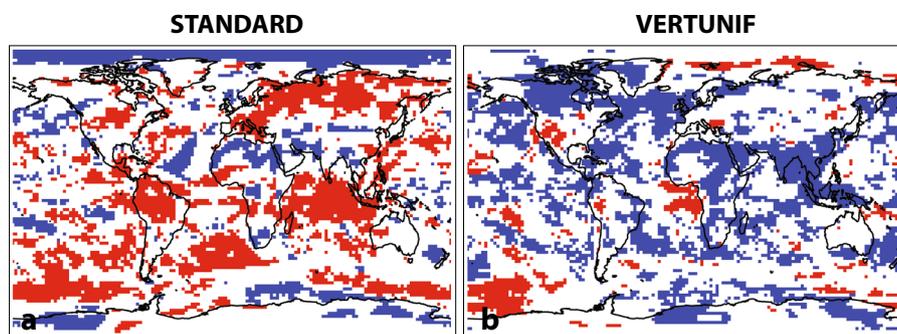
Fig. 5 Aerosol–cloud semi-direct effect model agreement. a Observationally constrained fine-mode aerosols without dust and sea salt (STANDARD); b analogous simulations with vertically uniform aerosol atmospheric heating (VERTUNIF). Regions where all three models agree on a positive (negative) SDE are colored red (blue)

consistent with the large negative temperature adjustment, including both tropospheric and stratospheric temperature adjustments. In contrast, warming in STANDARD peaks near 300 hPa and then decays aloft, with cooling above ~100 hPa exists. This implies a smaller (negative) tropospheric temperature adjustment and a positive stratospheric temperature adjustment. Thus, the large upper tropospheric/lower stratospheric warming in PDRMIP 10xBC simulations, which is consistent with the large amount of aerosol heating aloft (Fig. 1c), likely leads to a large negative tropospheric and stratospheric adjustment, and in turn, a large negative non-cloud adjustment.

Sensitivity simulations
To test the hypothesis that the cause of the SDE sign difference using observationally constrained aerosols, relative to PDRMIP and other aerosol simulations, is related to the vertical aerosol heating profile (Fig. 1), we perform sensitivity simulations with observationally constrained aerosol forcing, but we apply it uniformly in the vertical (VERTUNIF simulations). Figure 2 shows that VERTUNIF yields very different results relative to STANDARD, and moreover, VERTUNIF yields cloud changes very similar to PDRMIP. Relatively large increases in cloud and RH occur near the surface, extending up to ~800 hPa. Above ~800 hPa, decreases in both cloud and RH

exist, with relatively large reductions above ~300 hPa. Consistently, VERTUNIF yields increases in low cloud, decreases in mid-level cloud, and large decreases in high cloud (Table 1; Supplementary Fig. 6). Several regions of cloud response model agreement exist, particularly for high cloud (Supplementary Fig. 1). These changes are again consistent with ΔRH (Supplementary Discussion). Relative to STANDARD, VERTUNIF $RH_{925-700}$ now increases and $RH_{300-250}$ yields larger and more consistent decreases (Supplementary Table 1). In turn, the effective radiative forcing (ERF) swaps sign from positive to negative, as does the rapid adjustment and the aerosol cloud SDE (which still dominates the rapid adjustment). GFDL VERTUNIF yields an aerosol–cloud SDE of $-0.41\,m^{-2}$, which increases to $-0.67\,m^{-2}$ in CAM4 (Fig. 4d–f). SDE model agreement (Fig. 5b) also not only shows the dominance of a negative SDE, most notably over India and Southeast Asia, but also parts of Africa, Canada, and the North Atlantic. Moreover, the SDE is now dominated by longwave effects (cooling), consistent with the large decrease in high-level cloud. These results are also qualitatively consistent with other studies[13,25] that found weaker decreases in high cloud and a less negative SDE when BC above 200 and 500 hPa was restricted.

DISCUSSION

Using observationally constrained fine-mode aerosol forcing, we find a robust positive aerosol–cloud SDE, that acts to warm the climate system. This response is consistent with the corresponding cloud changes, including relatively large decreases in low- and mid-level cloud. Aerosol simulations, however, yield the opposite response—a negative SDE, primarily due to large decreases in high cloud and enhanced longwave cooling. These differences are related to the vertical profile of aerosol atmospheric heating, with aerosol simulations yielding a relatively vertically uniform profile, with strong heating that extends up to 100 hPa. The negative SDE and the corresponding cloud changes are qualitatively reproduced with a simple idealized simulation forced with observationally constrained aerosols, but with vertically uniform atmospheric heating.

We note that our approach has uncertainties of its own (Methods), including lack of consistency between the aerosol forcing and simulated meteorology, as well as the simulated cloud fields. The fine-mode aerosol radiative forcing is also subject to observational errors, including aerosol optical depth and aerosol optical properties, such as the single-scatter albedo.[39,40] Sensitivity tests were performed to quantify this uncertainty in observationally constrained fine-mode aerosol forcing,[37] resulting in an atmospheric heating uncertainty range of $\pm0.25\,W\,m^{-2}$. Uncertainty in CALIOP's aerosol vertical profile also exists, including attenuation of the lidar signal. For example, optically thick aerosol layers above African biomass burning can completely attenuate the signal, leading to no retrievals below these levels.[41] Our use of CALIOP's total aerosol vertical distribution, regardless of aerosol type, also leads to additional uncertainty in the absorbing aerosol vertical profile.

Our simulations show a large cloud response over southern Africa and southeast Atlantic (Fig. 3). Some studies have argued that over these regions (and other regions where absorbing aerosols are present), there are potential meteorological influences that confound aerosol–cloud interactions, such as the SDE.[42–46] For example, the presence of mid-tropospheric moisture and the southern Africa easterly jet correlate with the increase in the absorbing aerosols, and these meteorological changes appear to impact the cloud development over the southeast Atlantic, independent of the aerosol effect.[45,46] Although we have not attempted to formally separate dynamical versus thermodynamical impacts, we do show that cloud changes are generally consistent with the traditionally defined SDE and changes in relative humidity and stability (e.g., Fig. 2; Supplementary Table 2).

Nonetheless, a better understanding of how aerosol-induced changes in meteorology affect cloud responses is warranted.

Our focus has been to quantify the aerosol–cloud semi-direct effect based on anthropogenic aerosols, which is why the emphasis is on fine-mode aerosols without dust and sea salt. Although sea salt is a non-absorbing aerosol, dust is a weakly absorbing aerosol and thus has the potential to affect clouds via the semi-direct effect.[10,26,47] Moreover, some dust is anthropogenic in nature due to agricultural activities and land-use change.[48] Furthermore, climate change itself has likely perturbed dust emissions,[49,50] which also implies an anthropogenic contribution to dust. Our analysis does not account for possible dust-related SDE effects.

Although our observationally constrained aerosol forcing contains more atmospheric warming than model estimates, we find similar conclusions—including a positive SDE—with smaller atmospheric heating (HALF simulations). This is consistent with the importance of the vertical aerosol atmospheric heating profile, as opposed to its magnitude. Furthermore, global models may not be able to simulate sub-grid- scale features (e.g., cloud-layer thickness, cloud-top entrainment) that may influence the SDE. However, they should adequately simulate the large-scale features important for the SDE, including changes in stability and relative humidity, and modification of the large-scale atmospheric circulation. Thus, despite the caveats of our approach, we conclude that aerosol simulations lead to a negatively biased SDE. We also suggest that this bias may translate into other aspects of the climate response, including surface temperature and precipitation.

METHODS

Global climate models

This study uses the National Center for Atmospheric Research (NCAR) Community Atmosphere Model version 4 (CAM4)[34] and CAM5.[35] Both models have a horizontal resolution of 1.9° × 2.5°; CAM4 has 25 vertical layers and CAM5 has 30. Their main shared physical parameterization is the Zhang-McFarlane deep convection scheme (bulk mass flux with CAPE closure).[51] CAM4 uses a shallow convection scheme that involves three-level adjustment of moist static energy[52] and a prognostic single-moment microphysics scheme, including diagnostic cloud fraction.[53] Cloud fraction depends on several factors, including RH, S, water vapor, and convective mass fluxes. Three types of cloud are diagnosed: low-level marine stratus, convective cloud, and layered cloud. Layered clouds form when RH exceeds a pressure-dependent threshold. Marine stratocumulus clouds are diagnosed using an empirical relationship based on S. Convective cloud fraction is related to updraft mass flux in the deep- and shallow-cumulus schemes. The remaining cloud types are diagnosed on the basis of relative humidity.[34]

CAM5 uses a mass flux scheme with convective inhibition closure for shallow convection[54] and a prognostic double-moment microphysics scheme[55] with ice supersaturation[56] and a diagnostic cloud fraction scheme for cloud microphysics and macrophysics. Although deep-cumulus cloud fraction is diagnosed as in CAM4, shallow cumulus fraction in CAM5 is directly computed using the definition of convective updraft mass flux from the new shallow convection scheme. Liquid stratus fraction is derived from the assumed triangular distribution of the total relative humidity. The sensitivity of liquid stratus fraction to the changes of grid-mean RH differs between the two models. Ice stratus fraction is also diagnosed, using a modified version of Slingo's formula.

The rapid radiative transfer model (RRTMG) provides the radiative transfer calculations in CAM5, which is an accelerated and modified version of the correlated k-distribution model, RRTM.[57–59] RRTMG divides the solar spectrum into 14 shortwave bands that span 0.2 μm to 12.2 μm. A two-stream δ-Eddington approximation is used and assumes homogeneously mixed layers while accounting for absorption and scattering in the calculation of reflectance and transmittance. Distinction is made between the direct solar beam and scattered radiation. The calculation of shortwave radiation in CAM4 is based on a δ-Eddington approximation.[60–62] The solar spectrum is divided into 19 intervals, and the δ-Eddington solution for the reflectivity and transmissivity for each atmospheric layer under clear and

cloud skies is calculated. The layers are then combined together, accounting for multiple scattering between layers, allowing upward and downward spectral fluxes to be estimated.

We also use the Geophysical Fluid Dynamics Laboratory (GFDL) Atmospheric Model version 2.1 (AM2.1),[36] with a horizontal resolution of 2° × 2.5° and 24 vertical layers. Moist convection is represented by the Relaxed Arakawa–Schubert formulation.[63] In this parameterization, convection is represented by a spectrum of entraining plumes which produce precipitation. Closure is determined by relaxing the cloud work function for each cloud in the spectrum back to a critical value over a fixed time scale. Large-scale clouds are parameterized with separate prognostic variables for specific humidity of cloud liquid and ice, with an updated treatment of mixed-phase clouds.[64,65] Stratocumulus cloud cover is based on large-scale subsidence, diabatic cooling by radiation, and turbulent entrainment of warm and dry air from above the inversion.[66] Shortwave radiation is based on an exponential sum fit with 18 spectral bands.[67] The δ-Eddington method is used to solve for the layer reflection and transmission, while the thick-averaging method is used to combine layers.

Low-, mid-, and high-level clouds are directly calculated by each model. CAM4/5 assumes a maximum-random overlap, with low clouds based on pressure levels from the surface pressure to 700 hPa; mid-level clouds are based on 700–400 hPa; and high-level clouds are based on 400 hPa to the model top. For GFDL AM2.1, clouds are assumed to randomly overlap. Low clouds are calculated over 1000–680 hPa; mid-level clouds from 680 to 440 hPa and high clouds from 440 to 10 hPa. For PDRMIP models, these cloud diagnostics were not available for all models. Thus, low-, mid-, and high-level clouds are approximated as simple vertical averages of the cloud fractions over given pressure levels.[2] Low clouds are based on 1000–680 hPa; mid-level clouds are based on 680–440 hPa; and high clouds are based on 440–50 hPa. These are the same pressure levels used by ISCCP to define low-, mid-, and high-level clouds.

PDRMIP simulations

Ten global climate models simulated a control experiment using year 2000 greenhouse gas and aerosol concentrations or emissions, and an experiment in which anthropogenic BC concentration or emissions were increased by a factor of ten (10xBC).[2] Five models fixed their control BC concentrations to the monthly multi-model mean present-day concentration of AeroCom Phase II; the 10xBC experiment used a tenfold increase of this anthropogenic BC concentration. In the remaining five models, the control simulation was performed using present-day BC emissions, and the 10xBC experiment used a tenfold increase in the anthropogenic BC emissions. CESM-CAM4, GISS-E2-R, IPSL-CM5A, and NorESM1 are concentration driven; CanAM4, CESM-CAM5, HadGEM2-ES, and MIROC-SPRINTARS are emissions driven. Generally, present-day emissions refer to the year 2000; however, in the case of HadGEM2-ES, the year 1860 was used (the 10xBC experiment used a tenfold increase in anthropogenic BC emissions from the year 2000). All PDRMIP simulations analyzed here are based on an atmosphere-only setup, where sea surface temperatures are prescribed. Most simulations were performed for 15 years. The fast response of a tenfold increase in BC is obtained by taking the difference between the 10xBC experiment and the corresponding control simulation.

CESM1-CAM5 10xBC responses shown here are based on new simulations, analogous to PDRMIP. These new integrations include the double-radiation calls to estimate the instantaneous radiative forcing (which were missing from the original CESM1-CAM5-PDRMIP 10xBC simulation). The HadGEM2-ES instantaneous radiative forcing of 3.55 W m^{-2} also comes from a second ensemble member of the PDRMIP 10xBC experiment, and is somewhat different than that previously published (3.29 W m^{-2}).[2] This difference is due to internal variability and associated meteorological differences and aerosol transport between the two HadGEM2-ES ensemble members.

Experimental design

We conduct experiments with fixed sea surface temperature (fSST), which uses a repeating cycle of monthly climatological SSTs. The fSST setup prohibits significant global mean temperature change while keeping fast atmospheric responses, like the SDE. Experiments are run for 20 years, and the last 15 years are used in this study. Monthly observationally constrained fine-mode aerosol radiative effects (atmospheric heating rate and surface solar radiation reduction) are interpolated to each model's horizontal resolution and incorporated into their radiation modules. The atmospheric heating rate is vertically interpolated to each model's hybrid pressure levels. Although aerosol forcing is almost independent of solar

zenith angle (θ) when the angle is small, aerosol forcing approaches zero as θ approaches 90°. Thus, the added aerosol radiative effect is multiplied by a scaling factor that depends on zenith angle.[8,68] The climate response is estimated as the difference between the simulation with observationally constrained fine-mode aerosol (without dust and sea salt), and a corresponding control runs without observationally constrained fine-mode aerosol (STANDARD signal). The idealized vertically uniform heating simulations are analogous, but the monthly mean aerosol atmospheric heating is vertically averaged at each grid box, and this vertically averaged value is prescribed to all pressure levels >100 hPa. The climate response of vertically uniform heating (VERTUNIF signal) is obtained by taking a difference with the same control simulation. We also perform simulations analogous to STANDARD, but with half the aerosol forcing (HALF). At each grid box, the (monthly) reduction in surface solar radiation and atmospheric solar heating are reduced by 50%. Significance of all climate responses is based on a Student's t test for the difference of means, using the pooled variance.

In the case of the CAM4 and GFDL models, which only include aerosol-direct effects, the radiative effects of the default aerosols are neglected (in both observationally constrained aerosol and control simulations) by removing them from the list of radiatively active species. With CAM5, which includes both direct and indirect aerosol effects, the radiative effects of the default aerosols cannot be simply neglected. Thus, CAM5 simulations (observationally constrained and control) use prescribed (as opposed to prognostic) modal aerosols. Although this represents a double counting of aerosol effects in the observationally constrained CAM5 simulation, the response (observationally constrained minus control) will remove the bulk of the radiative effects due to the default prescribed aerosols (which will be similar in observationally constrained and control simulations).

Observationally constrained aerosol forcing

Aerosol optical depth (AOD) is a popular measure of aerosol amount, and known to be the most reliable global-scale aerosol product. However, the ground-based AErosol RObotic NETwork (AERONET) locations are heterogeneously distributed over the planet, while less reliable satellite AODs have nearly global coverage. Satellite AOD from the Moderate Resolution Imaging Spectroradiometer (MODIS) and Multi-angle Imaging Spectro-Radiometer (MISR) is therefore nudged toward AERONET AOD to obtain a globally reliable AOD from 2001 to 2010.[69,70] The AOD Angstrom exponent is also derived by adjusting the satellite AOD toward AERONET data. Fine-mode aerosol optical depth (fAOD) at 500 nm is obtained by using AERONET fAOD and the total AOD to derive the fine-mode fraction (FMF). The AOD Angstrom exponent data are converted into the FMF data, which are then nudged toward AERONET FMF data to derive reliable FMF and fAOD over the globe. Observational data gaps—which are primarily confined to polar regions—are filled by the Goddard Chemistry Aerosol Radiation and Transport (GOCART) model. GOCART accurately simulates most of the prominent AOD features in the satellite observations, within a factor of two for aerosol source and outflow areas.[71] However, several GOCART biases have been identified, including an underestimation of aerosol extinction over India, overestimation of aerosol extinction in dust source regions, and overestimation of aerosol aloft over mid-latitude transport regions.[72] Aerosol optical properties, such as the single-scatter albedo (SSA) and asymmetry parameter (ASY), are obtained by nudging GOCART SSA and ASY toward AERONET data.

Aerosol vertical profiles are obtained from the space-borne Cloud–Aerosol Lidar with Orthogonal Polarization (CALIOP).[33] CALIOP is able to distinguish between dust and other type of aerosols, which generally do not depolarize light, resulting in six aerosol categories, including dust, marine, smoke, polluted dust, polluted continental, and clean continental.[73] However, these aerosol categories were not used—the total aerosol vertical distribution was applied regardless of aerosol type. Daytime CALIPSO Level 2.0 data from June 2006 to October 2011 were processed to obtain a clear-sky aerosol extinction coefficient at 532 nm at the T42 spatial resolution and 500-m vertical resolution of the Monte Carlo Aerosol Cloud Radiation (MACR) model.[74,75] The data gaps are filled using available neighboring data through linear interpolation. A climatological seasonal cycle for the entire data period is then constructed. The aerosol vertical profile from CALIPSO is scaled to match the AOD observations obtained by integrating AERONET, MODIS, and MISR data.[37] To adjust the magnitude of AOD over cloud by CALIPSO data, 5° × 2° June 2006 to January 2012 globally gridded monthly mean daytime CALIPSO lidar Level 3.0 data[76] is used, specifically, the ratio of clear-sky AOD to above-cloud

AOD. This is used to modify the aerosol amount over cloud at each grid cell in the MACR model. For coarse-mode aerosols (which are not used here), the same vertical profiles are used. Because coarse-mode aerosols are not very absorbing, the effect on the vertical profile is very small.[75]

The direct aerosol effect is obtained by incorporating the integrated global aerosol data into an updated version of the MACR model.[37] MACR is based on the Monte Carlo Independent Column Approximation (McICA) and uses satellite observations to describe multilayer cloud, surface albedo, and stratospheric column ozone, as well as ERA-Interim Reanalyzes for precipitable water. The 2001–2010 surface albedo and stratosphere column ozone come from the Clouds and the Earth's Radiant Energy System (CERES) Synoptic Radiative Fluxes and Clouds (SYN) monthly product. Clouds come from the 2001–2010 averages of the merged daytime monthly mean CERES ISCCP-D2-like product, which is based on combined geostationary cloud retrievals and cloud retrievals from Terra/Aqua MODIS.[75] Clouds were combined into four types: low, mid, high, and convective clouds. Between the four types, a random overlap scheme was applied. The key element of this updated version is the Monte Carlo radiative transfer solver combined with the Monte Carlo integration in the multi-dimensional parameter space, including solar zenith angles, aerosol–cloud configurations, and spectral bands. Despite monthly resolution of the three-dimensional model inputs, MACR was run for all 365 days of the year to address variations in the solar zenith angle, declination, and eccentricity of Earth's orbit. For each day, 40,000 photons were deployed, and monthly inputs were interpolated in time and the model output was averaged over each month. The benefits of the Monte Carlo approach for radiative transfer is that it provides more accurate flux values relative to two stream approximations for both clear and cloudy skies.[77]

The global average atmospheric heating (F_{ATM}) and reduction in surface solar radiation (F_{SFC}) for fine-mode aerosols without dust and sea salt, which include both natural and anthropogenic aerosols, is $+3.64\,\mathrm{W\,m^{-2}}$ and $-3.75\,\mathrm{W\,m^{-2}}$, respectively ($-0.11\,\mathrm{W\,m^{-2}}$ TOA forcing). These estimates are several times larger than anthropogenic forcings estimated from models,[78] which are $0.75\,\mathrm{W\,m^{-2}}$ for F_{ATM} and $-1.02\,\mathrm{W\,m^{-2}}$ for F_{SFC}. This large difference is consistent with model underestimation of absorbing aerosol, including black carbon optical properties and emissions, as well as omission of absorbing brown carbon.[15,17–21] Furthermore, the observationally constrained F_{ATM} and F_{SFC} are larger over land than oceans. F_{ATM} is 2.67 (5.82) $\mathrm{W\,m^{-2}}$ over ocean (land) and F_{SFC} is -2.99 (-5.47) over ocean (land). Despite the relatively large aerosol forcing in STANDARD, we obtain similar conclusions—including cloud responses and a positive SDE—in our reduced aerosol-forcing simulation (HALF). This is consistent with the importance of the vertical aerosol atmospheric heating profile, as opposed to its magnitude.

We note that although this approach uses observations to constrain the fine-mode aerosol radiative effect, the results are subject to observation errors. AERONET SSA, in particular, is subject to uncertainties due to various assumptions used in the retrieval algorithms. Climatological AERONET SSA differs from in situ measured SSA by up to 0.02, with underestimation in low Ångström exponent areas and overestimation in high Ångström exponent areas.[40] The maximum error of AERONET AOD is between 0.01 and 0.015 for Level 2.0 data.[39] A direct validation of AERONET absorption AOD (AAOD) with unmanned aerial vehicle observations shows that AERONET AAOD errors are less than 20%.[79]

Sensitivity tests were performed to quantify the uncertainty (primarily due to AOD and SSA) in the observationally constrained fine-mode aerosol forcing used here.[37] Fine-mode aerosols yield atmospheric absorption of $3.88\,\mathrm{W\,m^{-2}}$. This varies from $3.63\,\mathrm{W\,m^{-2}}$ (least absorbing case) to $4.08\,\mathrm{W\,m^{-2}}$ (most absorbing case), yielding an uncertainty range of about $\pm 0.25\,\mathrm{W\,m^{-2}}$. These uncertainty estimates are based on modifying BC AOD and BC/organic aerosol (OA) SSA. Three different sets of simulated SSA are used:

$$SSA1 = (0.19 \mathrm{xBC\,AOD} + 0.85 \mathrm{xOA\,AOD} + \mathrm{sulfate\,AOD} + \mathrm{sea-salt\,AOD} + 0.96 \mathrm{xdust\,AOD})/\mathrm{total\,AOD}; \quad (1)$$

$$SSA2 = (0.14 \mathrm{xBC\,AOD} + 0.80 \mathrm{xOA\,AOD} + \mathrm{sulfate\,AOD} + \mathrm{sea-salt\,AOD} + 0.96 \mathrm{xdust\,AOD})/\mathrm{total\,AOD}; \mathrm{and} \quad (2)$$

$$SSA3 = (0.19 \mathrm{xBC\,AOD} + 0.98 \mathrm{xOA\,AOD} + \mathrm{sulfate\,AOD} + \mathrm{sea-salt\,AOD} + 0.96 \mathrm{xdust\,AOD})/\mathrm{total\,AOD}. \quad (3)$$

BC AOD above refers to the GOCART BC AOD at 550 nm. Parameters (e.g., 0.19 for BC SSA) in the above equations come from observational

studies.[80,81] In addition, in SSA2 (more absorbing case), the magnitude of BC AOD was doubled, given that simulated BC may be significantly underestimated.[15] These are then nudged toward the AERONET SSA, giving three sets of semi-observational SSA.[37] In terms of fine-mode dust and sea salt, with a baseline atmospheric heating estimate is $0.23\,\mathrm{W\,m^{-2}}$, sensitivity tests yield a corresponding uncertainty range from 0.16 to $0.26\,\mathrm{W\,m^{-2}}$. These sensitivity tests are based on using GOCART versus GISS ModelE2 fine-mode dust and sea salt.[37]

Uncertainty in the absorbing aerosol profile as derived from CALIPSO also exists, including attenuation of the lidar signal. For example, optically thick aerosol layers above African biomass burning can completely attenuate the signal, leading to no retrievals below these levels.[41] Although our observationally constrained aerosol vertical profile is not based on individual CALIPSO aerosol categories, such attenuation can also lead to misclassification of aerosol type by the classification algorithm.[82,83] However, our use of CALIPSO's total aerosol vertical distribution, regardless of aerosol type, also leads to additional uncertainty in the absorbing aerosol vertical profile. This uncertainty is much smaller than the overall differences between the CALIPSO profile and simulated BC profiles.

Semi-direct effect calculation

We account for aerosol radiative effects by incorporating the surface solar radiation reduction and atmospheric solar heating of observationally constrained fine-mode aerosol without dust and sea salt. This allows us to estimate the aerosol–cloud SDE using the traditionally defined cloud radiative flux (CRF)—the difference between top-of-the-atmosphere (TOA) net all-sky (SW) and clear-sky shortwave (SW_{clear}) and net all-sky (LW) and clear-sky (LW_{clear}) longwave radiative fluxes (i.e., $CRF = (SW - LW) - (SW_{clear} - LW_{clear})$). The SDE is the difference between the CRF from the observationally constrained aerosol experiment and the control run (i.e., $SDE = CRF_{experiment} - CRF_{control}$). In the case of PDRMIP simulations, one is unable to use the traditionally defined CRF, since a positive shortwave bias exists in the case of absorbing aerosol (by increasing the radiative warming when the absorbing aerosol lies above clouds).[38] Thus, it is necessary to use the clean-sky cloud radiative forcing, defined as $CRF_{clean} = (SW_{clean} - LW_{clean}) - (SW_{clean,clear} - LW_{clean,clear})$. Clean sky radiative fluxes are calculated as an additional diagnostic, but neglecting the scattering and absorption of radiation by all of the aerosol. As before, the SDE is estimated as $CRF_{clean,experiment} - CRF_{clean,control}$. Unfortunately, CAM4 and CAM5 are the only PDRMIP models to archive this diagnostic. Alternatively, if clear-sky instantaneous radiative forcing (IRF) is archived, the shortwave SDE can be estimated as $(\Delta ERF_{SW} - IRF) - (\Delta ERF_{SW,clear} - IRF_{clear})$, where ERF_{SW} is the effective radiative forcing in the shortwave ($SW_{experiment} - SW_{control}$) and the difference is between experiment (10xBC) and control simulations. The alternative approach allows us to calculate the SDE from HadGEM2-ES and MIROC-SPRINTARS. For MIROC-SPRINTARS, there will be an additional contribution from the indirect effect within this estimate. The aerosol–cloud indirect effect of black carbon on warm clouds is very small in MIROC-SPRINTARS, but the contribution of black carbon to ice clouds can be of importance.[84,85] CAM5 also includes aerosol–cloud interactions, but its magnitude in PDRMIP simulations has not been quantified.

The effective radiative forcing (ERF) is estimated as the difference in TOA radiative fluxes between aerosol simulation and control ($SW_{experiment} - LW_{experiment}$) − ($SW_{control} - LW_{control}$). The instantaneous radiative forcing (IRF) is estimated by an additional diagnostic call to the radiation scheme, but neglecting the scattering and absorbing of aerosols. The IRF is then the difference in TOA shortwave radiative fluxes, with and without aerosol direct effects ($SW - SW_{clean}$). The IRF of 10xBC is then $\Delta(SW - SW_{clean})$, where the difference is between experiment and control. Since $ERF = IRF + RAP_{ADJ}$, RAP_{ADJ} is estimated as $ERF - IRF$. Furthermore, IRF is negligible in the longwave, so $ERF_{LW} = RAP_{ADJ-LW}$. Rapid adjustments can be broken down into $SDE + residual$, where residual is related to changes in temperature and moisture (i.e., non-cloud adjustments). As long as the SDE is known, the residual can be subsequently estimated as $RAP_{ADJ} - SDE$.

Some discrepancies exist between the PDRMIP 10xBC SDE calculated here, and that calculated using radiative kernels and partial radiative perturbation (PRP) approaches.[4] Over our common PDRMIP models, our methodology yields a cloud adjustment (SDE) of $-0.41\,\mathrm{W\,m^{-2}}$ for MIROC-SPRINTARS, versus -0.29 to $-0.13\,\mathrm{W\,m^{-2}}$ using the radiative kernel and PRP method, respectively. For CESM1-CAM4, our approach yields $-1.05\,\mathrm{W\,m^{-2}}$ versus -0.66 to $-0.76\,\mathrm{W\,m^{-2}}$. For HadGEM2-ES, our approach yields $-1.26\,\mathrm{W\,m^{-2}}$ versus the the kernel method at $-0.44\,\mathrm{W\,m^{-2}}$, $-0.30\,\mathrm{W\,m^{-2}}$ for PRP and $-1.03\,\mathrm{W\,m^{-2}}$ using International Satellite Cloud Climatology

Project (ISCCP) cloud kernels.[86] Thus, relatively large uncertainty exists in the cloud adjustment, and the best method to evaluate it remains unresolved.

Discrepancies also exist in the residual term (i.e., non-cloud adjustment), related to changes in temperature and moisture. In our four PDRMIP models, the non-cloud adjustment ranges from -0.29 to $0.62\,W\,m^{-2}$, with a multi-model mean of $0.09\,W\,m^{-2}$. The corresponding shortwave (longwave) residual ranges from -0.04 to 0.32 (-0.36 to 0.52) $W\,m^{-2}$, with a multi-model mean of 0.11 (-0.03) $W\,m^{-2}$. These changes are generally consistent with enhanced water vapor leading to more solar absorption (positive shortwave residual) and atmospheric warming leading to enhanced longwave cooling (negative longwave residual). Exceptions do exist, however, including HadGEM2-ES, which exhibits a positive longwave rapid adjustment, which may be due to the stratospheric cooling simulated by this PDRMIP model.[2] In contrast to a weakly positive non-cloud adjustment using our approach, a negative non-cloud adjustment is obtained with the radiative kernel method.[4] Over the three common PDRMIP models, our methodology yields $-0.14\,W\,m^{-2}$ for MIROC-SPRINTARS versus $-0.24\,W\,m^{-2}$ for the radiative kernel method. For CESM1-CAM4, our approach yields $-0.29\,W\,m^{-2}$ versus $-0.56\,W\,m^{-2}$. The discrepancy is largest in HadGEM2-ES, where our approach yields $0.62\,W\,m^{-2}$ versus the radiative kernel method at $-0.53\,W\,m^{-2}$.

We note that the shortwave and longwave contributions to the cloud and non-cloud adjustments in PDRMIP are nearly always of the same sign between our method and the radiative kernel/PRP method. The main difference is that the cloud adjustment is more negative in our approach—primarily due to a larger negative longwave cloud adjustment. Our non-cloud adjustment, however, is less negative (positive in HadGEM2-ES)—primarily due to a weaker negative longwave non-cloud adjustment (positive in HadGEM2-ES). Since the total rapid adjustment is the same in both methods, the difference is in how we partition it into cloud versus non-cloud adjustments. Our approach of estimating the cloud adjustment may include a contribution from the non-cloud adjustment. This is because the non-cloud adjustment may be different in cloudy versus clear skies, but we have assumed it is independent of cloudy versus clear skies. Despite these differences, our major conclusions remain unaffected. Our approach yields a robust negative cloud adjustment in PDRMIP 10xBC simulations, as do the alternative methods,[4] and other studies with freely running aerosol simulations.[2,12–14] Furthermore, if our approach overestimates the negative cloud adjustment, this implies the positive cloud adjustment in STANDARD may be underestimated (more positive than what we show). STANDARD also yields cloud changes that are quite different than PDMRIP 10xBC (including decreases in low cloud, and much smaller decreases in high cloud), that are also consistent with differences in the aerosol vertical heating profile, and a positive cloud adjustment. VERTUNIF supports this conclusion, and the importance of the cloud adjustment to the total rapid adjustment, including the sign reversal. The cloud changes in VERTUNIF are similar to PDRMIP, and also consistent with a negative cloud adjustment. Thus, despite methodological differences in the cloud and non-cloud adjustment, our results still supports the notion that freely running aerosol simulations likely have a negatively biased aerosol–cloud SDE.

Although our analysis excludes dust, studies have shown that dust can exert an aerosol–cloud semi-direct effect. Observations were used to infer Saharan dust–marine stratocumulus interactions off the coast of northern Africa are likely dominated by the SDE.[26] In particular, a relatively large negative SDE was inferred during Northern Hemisphere summer, due to the presence of dust above the marine stratocumulus. During winter, however, dust and marine stratocumulus are co-located, and a positive (but weaker in magnitude) SDE was inferred. Modeling studies also suggest a dust induced SDE. For example, in regions with high dust load a significant increase in low cloud cover with increasing absorptivity of soil dust particles (except during Northern Hemisphere winter) was found.[10] Similarly, low-cloud cover (and precipitation) increased in response to dust radiative forcing over the western Sahara desert.[47] These increases in low cloud implies a negative SDE. However, a positive SDE due to dust has also been simulated.[87] Heating by dust may also impact convection (and the associated clouds). A 2D cloud resolving model showed lofted African dust yields low-level convergent flow toward the dust region and enhanced convection.[88] The adjacent, non-dusty regions experienced reduced convection.

In terms of our aerosol forcing estimates, fine-mode dust and sea salt yield a top of the atmosphere radiative forcing of $-0.35\,W\,m^{-2}$, decomposed into $+0.23\,W\,m^{-2}$ of atmospheric heating and $-0.58\,W\,m^{-2}$ of surface cooling.[37] The $+0.23\,W\,m^{-2}$ of atmospheric heating is quite small relative to fine-mode aerosol without dust and sea salt at $+3.64\,W\,m^{-2}$. This implies a relatively small SDE due to fine-mode dust and sea salt, although regional SDEs (e.g., Africa) may be larger. In terms of coarse-mode aerosols (mostly dust and sea salt), however, a top of the atmosphere radiative forcing of $-1.82\,W\,m^{-2}$ and an atmospheric heating of $+0.89\,W\,m^{-2}$ is obtained,[37] which is about 1/4 as large as the fine-mode aerosol, without dust and sea salt used here. Thus, based on our total (including coarse mode) dust atmospheric heating of $1.12\,W\,m^{-2}$, dust may have a substantial impact on the overall SDE, and this is not included here.

AUTHOR CONTRIBUTIONS
R.J.A. conceived the project, designed the study, performed model simulations, and wrote the paper. A.A. performed the bulk of the data analysis and wrote the paper. T.H. assisted with data analysis. J-F.L. performed the new CAM5-PDRMIP 10xBC simulations. C.S. supplied additional HadGEM2-ES data and cloud adjustment analyses. D.S. provided additional GISS-E2-R data. C.E.C. provided observationally constrained fine-mode aerosol data. All authors commented on the paper draft.

ADDITIONAL INFORMATION
Supplementary information accompanies the paper on the *npj Climate and Atmospheric Science* website (https://doi.org/10.1038/s41612-019-0073-9).

Competing interests: The authors declare no competing interests.

Publisher's note: Springer Nature remains neutral with regard to jurisdictional claims in published maps and institutional affiliations.

REFERENCES
1. Samset, B. H. et al. Fast and slow precipitation responses to individual climate forcers: A PDRMIP multimodel study. *Geophys. Res. Lett.* **43**, 2782–2791 (2016).
2. Stjern, C. W. et al. Rapid adjustments cause weak surface temperature response to increased black carbon concentrations. *J. Geophys. Res.: Atmospheres* **122**, 11,462–11,481 (2017).
3. Myhre, G. et al. PDRMIP: a precipitation driver and response model inter-comparison project—protocol and preliminary results. *Bull. Am. Meteorol. Soc.* **98**, 1185–1198 (2017).
4. Smith, C. J. et al. Understanding rapid adjustments to diverse forcing agents. *Geophys. Res. Lett.* **45**, 12023–12031 (2018).
5. Hansen, J., Sato, M. & Ruedy, R. Radiative forcing and climate response. *J. Geophys. Res.* **102**, 6831–6864 (1997).
6. Ackerman, A. S. et al. Reduction of tropical cloudiness by soot. *Science* **288**, 1042–1047 (2000).
7. Johnson, B. T., Shine, K. P. & Forster, P. M. The semi-direct aerosol effect: Impact of absorbing aerosols on marine stratocumulus. *Q. J. R. Meteorol. Soc.* **130**, 1407–1422 (2004).
8. Allen, R. J. & Sherwood, S. C. The aerosol-cloud semi-direct effect and land-sea temperature contrast in a GCM. *Geophys. Res. Lett.* **37**, L07702 (2010).
9. Koch, D. & Del Genio, A. D. Black carbon semi-direct effects on cloud cover: review and synthesis. *Atmos. Chem. Phys.* **10**, 7685–7696 (2010).
10. Perlwitz, J. & Miller, R. L. Cloud cover increase with increasing aerosol absorptivity–A counterexample to the conventional semidirect aerosol effect. *J. Geophys. Res. -Atmos.* **115**, D08203 (2010).
11. Randles, C. A., Colarco, P. R. & Silva, A. Direct and semi-direct aerosol effects in the NASA GEOS-5 AGCM: aerosol-climate interactions due to prognostic versus prescribed aerosols. *J. Geophys. Res.: Atmospheres* **118**, 149–169 (2013).
12. Mahajan, S., Evans, K. J., Hack, J. J. & Truesdale, J. E. Linearity of climate response to increases in black carbon aerosols. *J. Clim.* **26**, 8223–8237 (2013).
13. Hodnebrog, Ø., Myhre, G. & Samset, B. H. How shorter black carbon lifetime alters its climate effect. *Nat. Commun.* **5**, 5065 (2014).

14. Sand, M. et al. A standardized global climate model study showing unique properties for the climate response to black carbon aerosols. *J. Clim.* **28**, 2512–2526 (2015).

15. Bond, T. C. et al. Bounding the role of black carbon in the climate system: A scientific assessment. *J. Geophys. Res.* **118**, 5380–5552 (2013).

16. Boucher, O. et al. Clouds and Aerosols. In *Climate Change 2013: The Physical Science Basis. Contribution of Working Group I to the Fifth Assessment Report of the Intergovernmental Panel on Climate Change* (eds Stocker, T. F. et al.) 571–657 (Tech. Rep., Cambridge University Press, Cambridge, United Kingdom and New York, NY, USA, 2013).

17. Ramanathan, V. & Carmichael, G. Global and regional climate changes due to black carbon. *Nat. Geosci.* **1**, 221–227 (2008).

18. Koch, D. et al. Evaluation of black carbon estimations in global aerosol models. *Atmos. Chem. Phys.* **9**, 9001–9026 (2009).

19. Chung, C. E., Ramanathan, V. & Decremer, D. Observationally constrained estimates of carbonaceous aerosol radiative forcing. *Proc. Natl. Acad. Sci.* **109**, 11624–11629 (2012).

20. Cohen, J. B. & Wang, C. Estimating global black carbon emissions using a top-down Kalman Filter approach. *J. Geophys. Res.: Atmospheres* **119**, 307–323 (2014).

21. Myhre, G. & Samset, B. H. Standard climate models radiation codes underestimate black carbon radiative forcing. *Atmos. Chem. Phys.* **15**, 2883–2888 (2015).

22. Ming, Y., Ramaswamy, V. & Persad, G. Two opposing effects of absorbing aerosols on global-mean precipitation. *Geophys. Res. Lett.* **37**, L13701 (2010).

23. Zarzycki, C. M. & Bond, T. C. How much can the vertical distribution of black carbon affect its global direct radiative forcing? *Geophys. Res. Lett.* **37**, https://doi.org/10.1029/2010GL044555 (2010).

24. Ban-Weiss, G. A., Cao, L., Bala, G. & Caldeira, K. Dependence of climate forcing and response on the altitude of black carbon aerosols. *Clim. Dyn.* **38**, 897–911 (2012).

25. Samset, B. H. & Myhre, G. Climate response to externally mixed black carbon as a function of altitude. *J. Geophys. Res.: Atmospheres* **120**, 2913–2927 (2015).

26. Amiri-Farahani, A., Allen, R. J., Neubauer, D. & Lohmann, U. Impact of Saharan dust on North Atlantic marine stratocumulus clouds: importance of the semidirect effect. *Atmos. Chem. Phys.* **17**, 6305–6322 (2017).

27. Schwarz, J. P. et al. Global-scale black carbon profiles observed in the remote atmosphere and compared to models. *Geophys. Res. Lett.* **37**, L18812 (2010).

28. Allen, R. J. & Landuyt, W. The vertical distribution of black carbon in CMIP5 models: Comparison to observations and the importance of convective transport. *J. Geophys. Res.: Atmospheres* **119**, 4808–4835 (2014).

29. Koffi, B. et al. Evaluation of the aerosol vertical distribution in global aerosol models through comparison against CALIOP measurements: AeroCom phase II results. *J. Geophys. Res.: Atmospheres* **121**, 7254–7283 (2016).

30. Park, S. & Allen, R. J. Understanding influences of convective transport and removal processes on aerosol vertical distribution. *Geophys. Res. Lett.* **42**, 10,438–10,444 (2015).

31. Garrett, T. J., Zhao, C. & Novelli, P. C. Assessing the relative contributions of transport efficiency and scavenging to seasonal variability in arctic aerosol. *Tellus B* **62**, 190–196 (2010).

32. Liu, J., Fan, S., Horowitz, L. W. & Levy, H. Evaluation of factors controlling long-range transport of black carbon to the Arctic. *J. Geophys. Res.: Atmospheres* **116**, https://doi.org/10.1029/2010JD015145 (2011).

33. Liu, Z. et al. The CALIPSO lidar cloud and aerosol discrimination: version 2 algorithm and initial assessment of performance. *J. Atmos. Ocean. Technol.* **26**, 1198–1213 (2009).

34. Neale, R. B. et al. Description of the NCAR Community Atmosphere Model (CAM 4.0). Tech. Rep. NCAR/TN-???+STR, National Center for Atmospheric Research, Boulder, CO, 194 (2010).

35. Neale, R. B. et al. Description of the NCAR Community Atmosphere Model (CAM 5.0). Tech. Rep. NCAR/TN-486+STR, National Center for Atmospheric Research, Boulder, CO, 268 (2010).

36. Anderson, J. et al. The new GFDL global atmosphere and land model AM2-LM2: Evaluation with prescribed SST simulations. *J. Clim.* **17**, 4641–4673 (2004).

37. Chung, C. E. Global fine-mode aerosol radiative effect, as constrained by comprehensive observations. *Atmos. Chem. Phys.* **16**, 8071–8080 (2016).

38. Ghan, S. J. Technical note: estimating aerosol effects on cloud radiative forcing. *Atmos. Chem. Phys.* **13**, 9971–9974 (2013).

39. Eck, T. F. et al. Wavelength dependence of the optical depth of biomass burning, urban, and desert dust aerosols. *J. Geophys. Res. -Atmos.* **104**, 31,333–31,349 (1999).

40. Eck, T. F. et al. Climatological aspects of the optical properties of fine/coarse mode aerosol mixtures. *J. Geophys. Res. -Atmos.* **115**, D19205 (2010).

41. Das, S. et al. Biomass burning aerosol transport and vertical distribution over the South African-Atlantic region. *J. Geophys. Res. -Atmos.* **22**, 6391–6415 (2017).

42. Mauger, G. S. & Norris, J. R. Meteorological bias in satellite estimates of aerosol-cloud relationships. *Geophys. Res. Lett.* **34**, L16824 (2007).

43. Mauger, G. S. & Norris, J. R. Assessing the impact of meteorological history on subtropical cloud fraction. *J. Clim.* **23**, 2926–2940 (2010).

44. Davidi, A., Kostinski, A. B., Koren, I. & Lehahn, Y. Observational bounds on atmospheric heating by aerosol absorption: Radiative signature of transatlantic dust. *Geophys. Res. Lett.* **39**, L04803 (2012).

45. Adebiyi, A. A., Zuidema, P. & Abel, S. J. The convolution of dynamics and moisture with the presence of shortwave absorbing aerosols over the southeast atlantic. *J. Clim.* **28**, 1997–2024 (2015).

46. Adebiyi, A. A. & Zuidema, P. The role of the southern African easterly jet in modifying the southeast Atlantic aerosol and cloud environments. *Quart. J. R. Meteor. Soc.* **142**, 1574–1589 (2016).

47. Miller, R. L., Tegen, I. & Perlwitz, J. Surface radiative forcing by soil dust aerosols and the hydrologic cycle. *J. Geophys. Res. -Atmos.* **109**, D04203 (2004).

48. Ginoux, P., Prospero, J. M., Gill, T. E., Hsu, N. C. & Zhao, M. Global-scale attribution of anthropogenic and natural dust sources and their emission rates based on MODIS deep blue aerosol products. *Rev. Geophys.* **50**, RG3005 (2012).

49. Allen, R. J., Landuyt, W. & Rumbold, S. T. An increase in aerosol burden and radiative effects in a warmer world. *Nat. Clim. Change* **6**, 269–274 (2016).

50. Allen, R. J., Hassan, T., Randles, C. A. & Su, H. Enhanced land-sea warming contrast elevates aerosol pollution in a warmer world. Nat. Clim. Change. https://doi.org/10.1038/s41558-019-0401-4 (2019).

51. Zhang, G. J. & McFarlane, N. A. Sensitivity of climate simulations to the parameterization of cumulus convection in the canadian climate center general-circulation model. *Atmosphere-Ocean* **33**, 407–446 (1995).

52. Hack, J. Parameterization of moist convection in the National Center for Atmospheric Research Community Climate model (CCM2). *J. Geophys. Res.* **99**, 5551–5568 (1994).

53. Rasch, P. J. & Kristjánsson, J. E. A comparison of the CCM3 model climate using diagnosed and predicted condensate parameterizations. *J. Clim.* **11**, 1587–1614 (1998).

54. Park, S. & Bretherton, C. S. The University of Washington shallow convection and moist turbulence schemes and their impact of climate simulations with the community atmosphere model. *J. Clim.* **22**, 3449–3469 (2009).

55. Morrison, H. & Gettelman, A. A new two-moment bulk stratiform cloud micro-physics scheme in the community atmosphere model, version 3 (CAM3), Part I: description and numerical tests. *J. Clim.* **21**, 3642–3659 (2008).

56. Gettelman, A. et al. Global simulations of ice nucleation and ice supersaturation with an improved cloud scheme in the community atmosphere model. *J. Geophys. Res* **115**, D18216 (2010).

57. Mlawer, E. J., Taubman, S. J., Brown, P. D., Iacono, M. J. & Clough, S. A. Radiative transfer for inhomogeneous atmospheres: RRTM, a validated correlated-k model for the longwave. *J. Geophys. Res. -Atmos.* **102**, 16663–16682 (1997).

58. Clough, S. A. et al. Atmospheric radiative transfer modeling: A summary of the AER codes. *J. Quant. Spect. Rad. Transf.* **91**, 233–244 (2005).

59. Iacono, M. J. et al. Radiative forcing by long-lived greenhouse gases: calculations with the AER radiative transfer models. *J. Geophys. Res. -Atmos.* **113**, D13103 (2008).

60. Joseph, J. H., Wiscombe, W. J. & Weinman, J. A. The delta-Eddington approximation for radiative flux transfer. *J. Atmos. Sci.* **33**, 2452–2459 (1976).

61. Coakley, J. A., Cess, R. D. & Yurevich, F. B. The effect of tropospheric aerosols on the Earth's radiation budget: a paramterization for climate models. *J. Atmos. Sci.* **40**, 116–138 (1983).

62. Briegleb, B. P. Delta-eddington approximation for solar radiation in the NCAR Community Climate Model. *J. Geophys. Res. -Atmos.* **97**, 7603–7612 (1992).

63. Moorthi, S. & Suarez, M. J. Relaxed Arakawa-Schubert: a parameterization of moist convection for General Circulation Models. *Mon. Wea. Rev.* **120**, 978–1002 (1992).

64. Rotstayn, L. D. A physical based scheme for the treatment of stratiform clouds and precipitation in large-scale models. I: description and evaluation of the microphysical processes. *Q. J. R. Meteorol. Soc.* **123**, 1227–1282 (1997).

65. Rotstayn, L. D., Ryan, B. F. & Katzfey, J. J. A scheme for calculation of the liquid fraction in mixed-phase stratiform clouds in large-scale models. *Mon. Wea. Rev.* **128**, 1070–1088 (2000).

66. Tiedtke, M. Representation of clouds in large-scale models. *Mon. Wea. Rev.* **121**, 3040–3061 (1993).

67. Freidenreich, S. M. & Ramaswamy, V. A new multiple-band solar radiative parameterization for general circulation models. *J. Geophys. Res. -Atmos.* **104**, 31389–31409 (1999).

68. Chung, C. E. Steady vs. fluctuating aerosol radiative forcing in a climate model. *J. Korean Meteor. Soc.* **42**, 411–417 (2006).

69. Chung, C. E., Ramanathan, V., Kim, D. & Podgorny, I. A. Global anthropogenic aerosol direct forcing derived from satellite and ground-based observations. *J. Geophys. Res.* **110**, D24207 (2005).

70. Lee, K. & Chung, C. E. Observationally-constrained estimates of global fine-mode AOD. *Atmos. Chem. Phys.* **13**, 2907–2921 (2013).

71. Chin, M. et al. Tropospheric aerosol optical thickness from the GOCART model and comparisons with satellite and sunphotometer measurements. *J. Atmos. Sci.* **59**, 461–483 (2002).

72. Yu, H. et al. Global view of aerosol vertical distributions from CALIPSO lidar measurements and GOCART simulations: regional and seasonal variations. *J. Geophys. Res.: Atmospheres* **115**, https://doi.org/10.1029/2009JD013364 (2010).

73. Omar, A. H. et al. The CALIPSO automated aerosol classification and lidar ratio selection algorithm. *J. Atmos. Ocean. Technol.* **26**, 1994–2014 (2009).

74. Podgorny, I. A., Conant, W. C., Ramanathan, V. & Satheesh, S. K. Aerosol modulation of atmospheric and solar heating over the tropical Indian Ocean. *Tellus, Ser. B* **52**, 947–958 (2000).

75. Choi, J.-O. & Chung, C. E. Sensitivity of aerosol direct radiative forcing to aerosol vertical profile. *Tellus B* **66**, 24376 (2014).

76. Winker, D. M. et al. The global 3-D distribution of tropospheric aerosols as characterized by CALIOP. *Atmos. Chem. Phys.* **13**, 3345–3361 (2013).

77. Barker, H. W. et al. Assessing 1d atmospheric solar radiative transfer models: Interpretation and handling of unresolved clouds. *J. Clim.* **16**, 2676–2699 (2003).

78. Myhre, G. et al. Anthropogenic and Natural Radiative Forcing. In *Climate Change 2013: The Physical Science Basis. Contribution of Working Group I to the Fifth Assessment Report of the Intergovernmental Panel on Climate Change* (eds Stocker, T. F. et al.) 659–740 (Tech. Rep., Cambridge University Press, Cambridge, United Kingdom and New York, NY, USA, 2013).

79. Corrigan, C. E., Roberts, G. C., Ramana, M. V., Kim, D. & Ramanathan, V. Capturing vertical profiles of aerosols and black carbon over the Indian Ocean using autonomous unmanned aerial vehicles. *Atmos. Chem. Phys.* **8**, 727–747 (2008).

80. Magi, B. I. Chemical apportionment of southern african aerosol mass and optical depth. *Atmos. Chem. Phys.* **9**, 7643–7655 (2009).

81. Magi, B. I. Corrigendum to "chemical apportionment of southern African aerosol mass and optical depth". *Atmos. Chem. Phys.* **11**, 4777–4778 (2011).

82. Burton, S. P. et al. Aerosol classification from airborne HSRL and comparisons with the CALIPSO vertical feature mask. *Atmos. Meas. Tech.* **6**, 1397–1412 (2013).

83. Kacenelenbogen, M. et al. An evaluation of CALIOP/CALIPSO's aerosol?above? cloud detection and retrieval capability over North America. *J. Geophys. Res. -Atmos.* **119**, 230–244 (2014).

84. Takemura, T., Nozawa, T., Emori, S., Nakajima, T. Y. & Nakajima, T. Simulation of climate response to aerosol direct and indirect effects with aerosol transport-radiation model. *J. Geophys. Res.: Atmospheres* **110**, https://doi.org/10.1029/2004JD005029 (2005).

85. Takemura, T. et al. A simulation of the global distribution and radiative forcing of soil dust aerosols at the Last Glacial Maximum. *Atmos. Chem. Phys.* **9**, 3061–3073 (2009).

86. Zelinka, M. D., Klein, S. A. & Hartmann, D. L. Computing and partitioning cloud feedbacks using cloud property histograms. part i: cloud radiative kernels. *J. Clim.* **25**, 3715–3735 (2012).

87. Tegen, I. & Heinold, B. Large-scale modeling of absorbing aerosols and their semi-direct effects. *Atmosphere* **9**, 380 (2018).

88. Stephens, G. L., Wood, N. B. & Pakula, L. A. On the radiative effects of dust on tropical convection. *Geophys. Res. Lett.* **31**, L23112 (2004).